Check for updates

Complex master-slave for long axial range swept-source optical coherence tomography

MANUEL J. MARQUES,[1,*] **SYLVAIN RIVET,**[2] **ADRIAN BRADU,**[1] **AND ADRIAN PODOLEANU**[1]

[1]*Applied Optics Group, University of Kent, Canterbury CT2 7NH, Kent, UK*
[2]*Laboratoire d'Optique et de Magnétisme, Université de Bretagne Occidentale, IBSAM, 6 avenue Le Gorgeu, 29238 Brest Cedex 3, France*
[*]m.j.marques@kent.ac.uk

Abstract: Using complex master-slave interferometry, we demonstrate extended axial range optical coherence tomography for two commercially available swept sources, well beyond the limit imposed by their k-clocks. This is achieved without k-domain re-sampling and without engaging any additional Mach-Zehnder interferometer providing a k-clock signal to the digitizer. An axial imaging range exceeding 17 mm with an attenuation of less than 30 dB is reported using two commercially available swept sources operating at 1050 nm and a 100 kHz repetition rate. This procedure has more than trebled the range achievable using the k-clock signal provided by the manufacturers. An analysis is presented on the impact that the digitization has on the axial range and resolution of the system.

1. Introduction

In frequency-domain optical coherence tomography (FD-OCT) methods such as spectral-domain (SD-OCT) and swept-source OCT (SS-OCT), the largest optical path difference (OPD) where sufficiently strong interference signal is produced determines the maximum axial range. We refer to this as the optical limit of the axial range. When using SS-OCT, this optical limit is determined by the dynamic coherence length of the swept source. When using SD-OCT, the optical limit is determined by the coherence length of waves after diffraction in the spectrometer [1]. The dynamic coherence length of swept sources is generally much longer than the coherence length of the diffracted waves after diffraction in spectrometers, therefore SS-OCT exhibits a larger axial range than its SD-OCT counterpart.

In polarization-sensitive OCT systems a long axial range is particularly desirable since it is possible to multiplex several measurements by encoding them in the optical path difference [2]. Another example of a system with a large axial range was reported by Eugui *et al.* [3], where the collection of light returned from the sample was performed using a multi-mode fiber. This allowed several modes to be guided with different mode velocities, again leading to encoding of different sample orientation angles on the OPD values. Recently, novel VCSEL-based tunable sources with meter-sized coherence lengths have been reported [4], which allow for large-scale, meter-sized imaging. Such sources can also prove useful in obtaining vascularization maps of large sections of tissue, such as those reported by Xu *et al.* [5,6].

The larger the OPD, the denser the modulation of the spectrum at the OCT interferometer output, therefore, in practice, digitizers with high sampling rates are needed. Therefore, the maximum frequency sampling rate of the digitizer [7] establishes a digital axial range limit. With the increase in the sweeping speed, long coherence length swept sources demand multi-GS/s sampling rates. Due to the high cost of digitizers and the requirement to produce a GHz-range k-clock signal (to perform the k-domain linearization), the majority of reports on SS-OCT are limited to an axial range of $3-5$ mm. Effectively, the k-clock frequency dictates the sampling

rate of the digital acquisition that ultimately limits the axial range. Usually, and particularly in commercially-available optical sources, this is less than the dynamic coherence length of the swept source.

In order to attain a longer axial range, strategies bypassing the source's built-in k-clock have been reported. An additional Mach-Zehnder interferometer (MZI) with a large OPD between the MZI arms, coupled with a high-speed photodetector to produce a k-clock signal at higher frequencies [4,8,9] were reported. As a different alternative, software-based k-domain re-sampling procedures [10] have also been used. These procedures impact the performance of the system by requiring the data to be re-sampled prior to FFT. It is possible to improve the software-based re-sampling procedures in terms of speed by implementing them via GPUs [11] or FPGAs [12]. A totally different method is employed here, the Complex Master-Slave (CMS-OCT) method reported by our group [13] it has been shown that there are some performance gains, namely in terms of processing speed, when compared to the conventional procedure of software-based re-sampling followed by FFT. CMS-OCT works by performing a comparison of the acquired spectrum from the OCT interferometer output against a set of spectra called masks. For each point along the axial range needed, a comparison operation is performed with such a mask [14]. Masks are inferred from a few previously acquired spectra [15], according to the algorithm presented in Rivet *et al.* [13]. Since both inferred spectra and those used for imaging are produced by the same interferometer, they are similarly affected by the tuning non-linearities of the swept source and by the dispersion in the interferometer. Therefore, there is no need to perform a re-sampling step, and additionally no dispersion compensation between the two arms of the interferometer is necessary, as described previously [16].

In Bradu *et al.* [17] the CMS-OCT method has been employed with an Axsun tunable source coupled to an optical interferometer set up to take advantage of the coherence revival property present in these optical sources. Similarly to that reported earlier by Dhalla *et al.* [18,19], this property allows for the maximum of the sensitivity profile to be shifted away from OPD = 0. This leads to an increase in the effective axial range of the SS-OCT system. However, this method does introduce a slight sensitivity penalty [18], and it is only applicable to a select number of optical sources.

In this paper, we report on the possibility of utilizing the axial imaging range up to its optical limit, as allowed by the dynamic coherence length of the swept source, using the CMS-OCT technology. This is demonstrated here using two commercially available swept source lasers operating in the 1-micron region with no coherence revival. By not utilizing the k-clock function and maximizing the sampling rate of the electronic digitizer, we demonstrate up to 17 mm imaging range, well above the 3.7 mm [20] and 4.0 mm [21] imposed by each source's k-clock. We compared our approach against the typical usage scenario employing the k-clock of the optical source supplied by the manufacturer.

2. Experimental set-up

The system used is schematically represented in Fig. 1. Light from the swept source (100 kHz A-line rate, 1.06 μm central wavelength; either Axsun Technologies OCT Engine , Billerica, MA, USA or Santec HSL-10-100, Aichi, Japan) is split between the two arms of the interferometer at the first fiber-based coupler (DC1). Light from the sample arm is then re-coupled with the light from the reference arm (operating in transmission) at the second fiber-based coupler (DC2). A balanced photo-detector (Thorlabs PDB481C-AC (Newton, NJ, USA), 1.0 GHz, optimized for 1.06 μm) delivers the signal to an electrical high-pass filter (Thorlabs EF515 (Newton, NJ, USA), >10 MHz) that performs some conditioning on the interferogram. The resulting signal is then sent to a high-speed digitizer board (ATS, AlazarTech ATS9360 (Pointe-Claire, Québec, Canada), up to 1.8 GS/s sampling rate, 800 MHz input bandwidth). A high-speed digital storage oscilloscope (DSO, LeCroy WaveRunner 104MXi (Chestnut Ridge, NY, USA), up to 10 GS/s
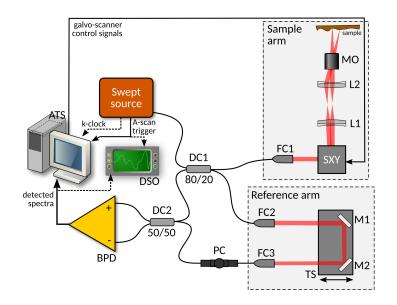
Fig. 1. Swept-source OCT system used to demonstrate the long axial range CMS interferometry procedure. DC1-2: fiber-based directional couplers; FC1-3: fiber collimators; SXY: pair of galvo-scanners (Cambridge Technologies, model 6110); L1-2: achromatic lenses forming a telecentric configuration; MO: microscope objective; M1-2: flat protected silver mirrors; BPD: balanced photo-detector; PC: fiber-based inline polarization controller; TS: translation stage; ATS: AlazarTech ATS9360 digitizer board (inside computer); DSO: digital storage oscilloscope.

sampling rate, 1 GHz input bandwidth) is also employed to monitor the detected optical power during the measurements and also to perform additional characterization of the channeled spectra due to its higher sampling frequency.

In order to fully characterize the channeled spectrum visibility variation with the OPD, a flat silver mirror is placed in the focal plane of the objective lens MO. To vary the OPD, the reference arm length is then adjusted by moving an assembly containing M1 and M2, placed on a motorized translation stage TS (Newport M-VP-25XA, 25 mm travel range, connected to MM4006 controller). Channeled spectra are then collected at each position of TS, which is varied in steps of 0.5 mm. The procedure is carried out with either the digitizer card configured at several sampling rates or with the 1 GHz digital storage oscilloscope (DSO) sampling each channeled spectrum acquired within each swept source sweep of ~ 10 μs at 5 GS/s.

3. Results and discussion

The channeled spectra are processed using the CMS method, as described in Rivet *et al.* [13]. For each channeled spectrum acquired, the corresponding peak of the A-scan is located and its amplitude and width represented against the TS position, which can be linked to an OPD value. The full data sets are represented in Figs. 2 and 3. For determining the peak width, a peak width estimation algorithm is run for each A-scan and the peak full width at half maximum (FWHM) determined, allowing an estimation of the axial resolution at each depth considered.

As it can be observed in Fig. 2(a), when the k-clock from the optical source is used for the data acquisition, the imaging depth is significantly reduced. For the Axsun source, with a maximum k-clock frequency of 350 MHz, the maximum imaging range is 3.7 mm [point (i) in Fig. 2(a)]. The k-clock for the Santec source has a slightly higher maximum frequency, at 400 MHz, which
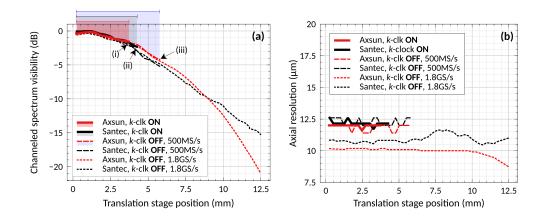
Fig. 2. (a) Channeled spectrum (CS) visibility versus TS position (obtained with the CMS method), measured for the case with the k-clock enabled (continuous lines) and for two other data sets with the k-clock disabled, acquired with a digital sampling rate of 500 MS/s (large dashes) and 1.8 GS/s (short dashes); red trace: Axsun source; black trace: Santec source. The shaded regions denote the axial range attainable with the Axsun using the k-clock (red), the Santec using the k-clock (grey), and either source without the k-clock and a 500 MS/s sampling rate (light blue). (b) Axial resolution estimated from the A-scan peak FWHM for the same cases described in (a).

increases the maximum imaging range to just over 4 mm [point (ii) in Fig. 2(a)]. In either case, the drop in the visibility profile at the maximum imaging range is small (under −2.5 dB), which is aided by the long coherence length reported by the manufacturers of these sources [20, 21].

Figure 2 also contains the channeled spectrum visibility profile and axial resolution traces obtained with data acquired without the source k-clock, using digital sampling rates of either 500 MS/s or 1.8 GS/s. With regards to the visibility profiles, it is clear that the traces generated from the data sets acquired without the k-clock follow the traces generated using the k-clock up to their maximum imaging range. The decay is determined by the combined effect of linewidth (dynamic coherence length) and signal digitization. The decay due to the dynamic coherence length is somehow uniform over the axial range, as interference strength is determined by the amount of overlap of two delayed wavetrains. The larger the OPD, the larger such delay and less overlap of the wavetrains occurs. In opposition to this continuous decay, that determined by digitization is mainly noticeable close to the digital limit. Therefore, at shallow depths, it is expected that the decay is solely dominated by the dynamic coherence length.

To show the behavior of the system when no k-clock is used, while at the same time maintaining a similar axial range to the case where the k-clock is used, a sampling rate of 500 MS/s is used (depending on the source used, k-clock frequency is between $350 − 400$ MHz). Point (iii) in Fig. 2(a) shows the imaging depth possible with such a configuration, just under 6 mm with a penalty on the visibility profile at that depth of just over −4 dB.

At the maximum sampling rate allowed by the digitizer card, 1.8 GS/s, the imaging range extends beyond the horizontal scale of Fig. 2(a); the full characterization is presented in Fig. 3.

With regards to the axial resolution of the system, it is clear from Fig. 2(b) that the evolution of the peak width with OPD is not significant for the data sets with the k-clock on. The same can be said for the data acquired with the k-clock off and sampled at 500 MS/s. For the data sets sampled at 1.8 GS/s, the axial resolution remains reasonably constant at $10 − 12\,\mu$m throughout the range. There is a difference in the behavior of the two sources for the same sampling rate, with the axial resolution for the Santec (black dashed trace) oscillating between 11 and 12 μm

throughout the interval of TS positions considered, while the axial resolution for the Axsun (red dashed trace) remains roughly constant at 10 μm.

The difference in the baseline axial resolution between the k-clock, 500 MS/s and the 1.8 GS/s data sets can be explained by the digitized spectra not covering exactly the same tuning range of the source, with the first two cases (k-clock on or off, with 500 MS/s sampling rate) covering a shorter spectral range interval, yielding a slightly worse axial resolution (12.5 μm).
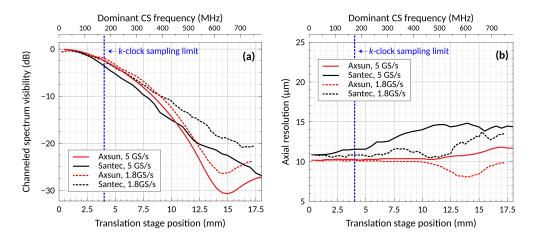

Fig. 3. (a) Channeled spectrum (CS) visibility versus TS position (obtained with the CMS method), measured for the data sets acquired with either the DSO (continuous lines) and the ATS sampling at 1.8 GS/s (dashed lines); red traces correspond to the Axsun source, whereas black traces correspond to the Santec source. (b) Axial resolution estimated from the A-scan peak FWHM for the same cases described in (a). Top axis shows the dominant (peak) frequency in the channeled spectrum for each TS position, obtained via a FFT-based analysis. Blue vertical line in either plot shows the axial imaging limit imposed by the k-clock (350 MHz, corresponding to a channeled spectrum frequency of 175 MHz).

In addition to the full axial range (over 17 mm) allowed by ATS when configured to its maximum sampling rate (1.8 GS/s), Fig. 3 also represents the visibility profiles and axial resolution obtained for either source when data is acquired with the DSO. By having a larger digital sampling rate (5 GS/s) and also a higher input bandwidth than the ATS, the DSO would be expected to reach longer imaging depths. Despite that, the curves in Fig. 3(a) exhibit higher visibility for the ATS at the same OPD. This may be due to the limited bit depth resolution of the DSO (8-bit) against the 12-bit depth of the ATS.

With either the DSO or the ATS we are able to reach over 17 mm imaging range for both sources, as shown in Fig. 3(a). However, some care must be taken in the interpretation of these results. Effectively, the cut-off frequencies for the balanced photo-detector, the ATS and the DSO are respectively 1 GHz, 800 MHz and 1 GHz.

By performing a frequency analysis of the channeled spectra acquired at several positions of the TS, one can establish a correspondence between OPD and the dominant frequency within each channeled spectra, as presented in Fig. 4. This frequency/TS position scale is represented above plots (a) and (b) in Fig. 3. The range covered finishes just before the 800 MHz mark, therefore one is to expect some artefacts and attenuation on the data sets acquired with the ATS board, whose input bandwidth is 800 MHz.

It is observed in Fig. 3(b) that the axial resolution variation with depth for the Santec source is more pronounced than that of the Axsun source, even if the axial resolution does not decrease by more than 50% in relation to the 10 μm baseline throughout the whole measurement range.
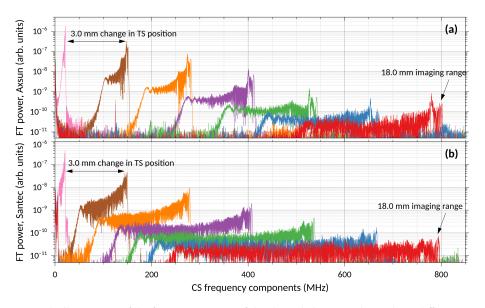
Fig. 4. Comparison of the frequency spectra of the channeled spectra obtained at 7 different OPDs (with a spacing of 3.0 mm between them) for the Axsun source [top plot, (a)] and for the Santec source [bottom plot, (b)]. All data sets sampled with the DSO, set at 5 GS/s sampling rate.

We conjecture that this behavior might be related to the increased chirping due to the tuning non-linearities exhibited by the Santec source, as shown by the frequency spectra presented in the plot in Fig. 4. For the same TS position, the channeled spectrum measured with the Santec seems to have a frequency spread nearly twice as large as the one from Axsun.

There is also an appreciable difference between the data sets acquired with each source and different digitization devices (ATS vs DSO). We conjecture that this may be also related with the different digitization bit depth between the two devices, as if one compares the drop between the brown and red traces in either plot of Fig. 4, there are more than 3 orders of magnitude in between them. Considering that the DSO is only capable of 8-bit digitization resolution (256 levels), that could explain the increased attenuation at large OPDs and the progressive degradation of the axial resolution (as the noise floor is comparable to the signal level at these large OPDs, especially with limited digitization resolution).

It is important to note that, despite the slight resolution degradation, we are able to still locate the peaks beyond the limits introduced by the BPD, ATS or DSO; there is no aliasing effect, just some channeled spectrum attenuation and potential deviation from the complex masks calculated during the calibration step of the CMS algorithm, since we are operating under the Nyquist limit (900 MHz for the ATS, using a sampling rate of 1.8 GS/s). The locations of the peaks were found through the CMS algorithm and cross-checked with the positions of the TS throughout the whole data acquisition process.

To further demonstrate the possibility of increasing the imaging range to the optical limit when not using the k-clock, our system was employed to image a retinal phantom (OCT Model Eye, Rowe Technical Design, Orange County, CA, USA). In order to simulate an object which would require a long imaging range, the reference arm length is varied multiple times, with a B-scan acquired at every TS position; then, a composite image is created which overlays all the B-scans, individually registered at each axial position as defined by TS. Naturally, the confocal gate remains in the same position; this experiment is only meant to assess the extended axial range imaging performance of the source and the optical interferometer when employed in
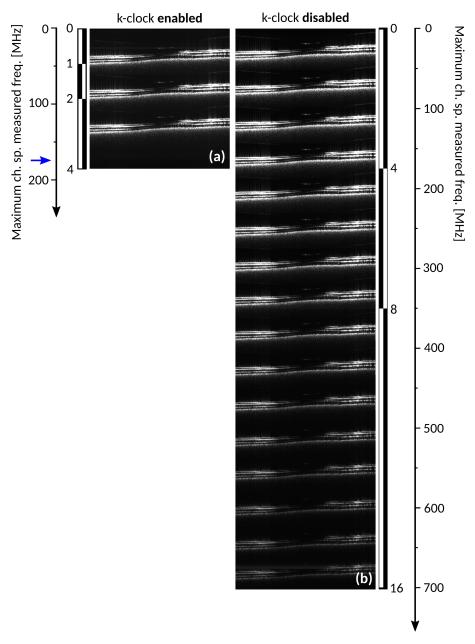
Fig. 5. Composite image generated from multiple B-scans, each taken at a different OPD setting with the Axsun source (separated by 1 mm in between B-scans). (a) B-scans acquired while using the source k-clock; (b) B-scans acquired by sampling the data at 1.8 GS/s using the ATS clock instead of the swept source k-clock. Scale bar units: mm. Transversal span is ~ 1 mm. Blue arrow: maximum frequency attainable with the k-clock of the Axsun source (175 MHz, corresponding to a sampling rate of 350 MHz).

conjunction with CMS and no k-clock. The two composite images (with and without the k-clock) are represented in Fig. 5(a) and 5(b), respectively.

It is clear that the two images present significantly different axial range values, mimicking the

behavior observed in Figs. 2 and 3. Despite a significant reduction in the overall brightness, it is still possible to resolve the bottom layers of the artificial macula even at depths over 14 mm, which is around the range of the ATS ADC clock frequency of 800 MHz. The layer mimicking the choroid is visible throughout the whole range of the composite image in Fig. 5(b). The bottom image in Fig. 5 (a) is still considerably brighter than the bottom one in Fig. 5(b), which again is in line with the behavior observed in the set of curves in Figs. 2 and 3.

4. Conclusions

In conclusion, we have demonstrated that the MS-OCT processing, when coupled with a high-throughput digitizer card is capable of achieving an imaging range close to the optical limit determined by the inverse of the source dynamic linewidth. The method here demonstrated bypasses the limitations introduced by the source built-in k-clock.

This study responds to the recent interest shown in long axial range imaging [2, 3] using long coherence length swept sources. This however has to be complemented by using either low NA interface optics in the sample arm or Bessel beams [22, 23]. If a high NA interface optics is needed, then this method can be combined with a Gabor fusion strategy [24, 25].

Funding

References

1. A. G. Podoleanu, "Optical coherence tomography," J. Microsc. **247**, 209–219 (2012).
2. Z. Wang, H.-C. Lee, O. O. Ahsen, B. Lee, W. Choi, B. Potsaid, J. Liu, V. Jayaraman, A. Cable, M. F. Kraus *et al.*, "Depth-encoded all-fiber swept source polarization sensitive OCT," Biomed. Opt. Express **5**, 2931–2949 (2014).
3. P. Eugui, A. Lichtenegger, M. Augustin, D. J. Harper, M. Muck, T. Roetzer, A. Wartak, T. Konegger, G. Widhalm, C. K. Hitzenberger, A. Woehrer, and B. Baumann, "Beyond backscattering: optical neuroimaging by BRAD," Biomed. Opt. Express **9**, 2476–2494 (2018).
4. Z. Wang, B. Potsaid, L. Chen, C. Doerr, H.-C. Lee, T. Nielson, V. Jayaraman, A. E. Cable, E. Swanson, and J. G. Fujimoto, "Cubic meter volume optical coherence tomography," Optica **3**, 1496–1503 (2016).
5. J. Xu, S. Song, S. Men, and R. K. Wang, "Long ranging swept-source optical coherence tomography-based angiography outperforms its spectral-domain counterpart in imaging human skin microcirculations," J. Biomed. Opt. **22**, 116007 (2017).
6. J. Xu, S. Song, W. Wei, and R. K. Wang, "Wide field and highly sensitive angiography based on optical coherence tomography with akinetic swept source," Biomed. Opt. Express **8**, 420–435 (2017).
7. J. A. Izatt, M. A. Choma, and A.-H. Dhalla, "Theory of optical coherence tomography," in *Optical Coherence Tomography: Technology and Applications,* (Springer, 2015), chap. 2, pp. 65–94.
8. B. Johnson, W. Atia, M. Kuznetsov, C. Cook, B. Goldberg, B. Wells, N. Larson, E. McKenzie, C. Melendez, E. Mallon, S. Woo, R. Murdza, P. Whitney, and D. Flanders, *Optical Coherence Tomography: Technology and Applications* 2nd ed. (Springer, 2015), chap. 21, p. 639.
9. K. Liang, O. O. Ahsen, Z. Wang, H.-C. Lee, W. Liang, B. M. Potsaid, T.-H. Tsai, M. G. Giacomelli, V. Jayaraman, H. Mashimo, X. Li, and J. G. Fujimoto, "Endoscopic forward-viewing optical coherence tomography and angiography with MHz swept source," Opt. Lett. **42**, 3193–3196 (2017).
10. S. Makita, T. Fabritius, and Y. Yasuno, "Full-range, high-speed, high-resolution 1-μm spectral-domain optical coherence tomography using BM-scan for volumetric imaging of the human posterior eye," Opt. Express **16**, 8406–8420 (2008).
11. S. Van der Jeught, A. Bradu, and A. G. Podoleanu, "Real-time resampling in Fourier domain optical coherence tomography using a graphics processing unit," J. Biomed. Opt. **15**, 030511 (2010).
12. T. E. Ustun, N. V. Iftimia, R. D. Ferguson, and D. X. Hammer, "Real-time processing for Fourier domain optical coherence tomography using a field programmable gate array," Rev. Sci. Instrum. **79**, 114301 (2008).
13. S. Rivet, M. Maria, A. Bradu, T. Feuchter, L. Leick, and A. Podoleanu, "Complex master slave interferometry," Opt. Express **24**, 2885–2904 (2016).

14. A. G. Podoleanu and A. Bradu, "Master–slave interferometry for parallel spectral domain interferometry sensing and versatile 3D optical coherence tomography," Opt. Express **21**, 19324–19338 (2013).

15. M. J. Marques, S. Rivet, A. Bradu, and A. G. Podoleanu, "Novel software package to facilitate operation of any spectral (Fourier) OCT system," in *European Conference on Biomedical Optics,* (Optical Society of America, 2017), p. 104160B.

16. A. Bradu, M. Maria, and A. G. Podoleanu, "Demonstration of tolerance to dispersion of master/slave interferometry," Opt. Express **23**, 14148–14161 (2015).

17. A. Bradu, S. Rivet, and A. Podoleanu, "Master/slave interferometry–ideal tool for coherence revival swept source optical coherence tomography," Biomed. Opt. Express **7**, 2453–2468 (2016).

18. A.-H. Dhalla, D. Nankivil, and J. A. Izatt, "Complex conjugate resolved heterodyne swept source optical coherence tomography using coherence revival," Biomed. Opt. Express **3**, 633–649 (2012).

19. A.-H. Dhalla, D. Nankivil, T. Bustamante, A. Kuo, and J. A. Izatt, "Simultaneous swept source optical coherence tomography of the anterior segment and retina using coherence revival," Opt. Lett. **37**, 1883–1885 (2012).

20. Axsun Technologies, "Swept lasers for OCT: 1060 & 1310 nm high speed swept laser engines," Online. Last checked: 22 Sept 2017.

21. Santec Corporation, "MEMS Based Swept Source HSL-10/20," Last accessed: 23 Jul 2018.

22. Z. Ding, H. Ren, Y. Zhao, J. S. Nelson, and Z. Chen, "High-resolution optical coherence tomography over a large depth range with an axicon lens," Opt. Lett. **27**, 243–245 (2002).

23. R. Leitgeb, M. Villiger, A. Bachmann, L. Steinmann, and T. Lasser, "Extended focus depth for Fourier domain optical coherence microscopy," Opt. Lett. **31**, 2450–2452 (2006).

24. J. P. Rolland, P. Meemon, S. Murali, K. P. Thompson, and K.-S. Lee, "Gabor-based fusion technique for optical coherence microscopy," Opt. Express **18**, 3632–3642 (2010).

25. R. Cernat, A. Bradu, N. M. Israelsen, O. Bang, S. Rivet, P. A. Keane, D.-G. Heath, R. Rajendram, and A. Podoleanu, "Gabor fusion master slave optical coherence tomography," Biomed. Opt. Express **8**, 813–827 (2017).